An Overview of the Semi-Span Super-Sonic Transport (S^4T) Wind-Tunnel Model Program

Walter A. Silva, * Boyd Perry III, † James R. Florance, ‡ Mark D. Sanetrik,‡
Carol D. Wieseman,‡ William L. Stevens,‡
Christie J. Funk §
NASA Langley Research Center, Hampton, Virginia, 23681
Jiyoung Hur ¶
David M. Christhilf¶
Lockheed-Martin, Hampton, Virginia, 23681
David A. Coulson ‖
Analytical Services and Materials, Hampton, Virginia, 23681

A summary of computational and experimental aeroelastic (AE) and aeroservoelastic (ASE) results for the Semi-Span Super-Sonic Transport (S^4T) wind-tunnel model is presented. A broad range of analyses and multiple AE and ASE wind-tunnel tests of the S^4T wind-tunnel model have been performed in support of the ASE element in the Supersonics Program, part of the NASA Fundamental Aeronautics Program. This paper is intended to be an overview of multiple papers that comprise a special S^4T technical session. Along those lines, a brief description of the design and hardware of the S^4T wind-tunnel model will be presented. Computational results presented include linear and nonlinear aeroelastic analyses, and rapid aeroelastic analyses using CFD-based reduced-order models (ROMs). A brief survey of some of the experimental results from two open-loop and two closed-loop wind-tunnel tests performed at the NASA Langley Transonic Dynamics Tunnel (TDT) will be presented as well.

I. Introduction

The unique structural configuration of supersonic aircraft combined with nonlinear aerodynamics and rigid-body effects often results in highly complex nonlinear aeroelastic/flight dynamics phenomena. These aeroelastic phenomena can affect ride quality, gust loads, flutter, flight dynamics and control, and engine performance. The aeroelastic/flight dynamics phenomena simultaneously influence the airframe and propulsion system controls, producing undesirable effects on performance and flying characteristics.

These ASE phenomena need to be thoroughly understood in order for supersonic flight to be safe, efficient, and comfortable. In addition, there is an opportunity, through active controls, to exploit these phenomena for improved performance and efficiency. Analysis and design capabilities for slender supersonic aircraft may then be enhanced by including this new knowledge.

A vast body of analytical, computational, wind-tunnel and flight data exist on the ASE characteristics of subsonic transport and supersonic fighter aircraft.[1] Systems for control of undesirable aeroelastic phenomena,

*Senior Research Scientist, Aeroelasticity Branch, AIAA Associate Fellow.
†Assistant Branch Head, Aeroelasticity Branch, AIAA Senior Member.
‡Aerospace Engineer, Aeroelasticity Branch, AIAA Senior Member.
§Graduate Student, Aeroelasticity Branch, AIAA Member.
¶Aerospace Engineer, AIAA Senior Member.
‖Controls Engineer.

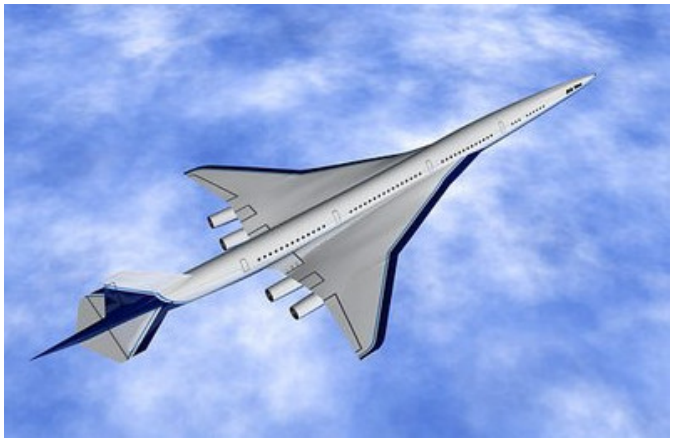

Figure 1. An artist's rendering of the Technology Concept Aircraft (TCA).

such as suppression of flutter, have been demonstrated in the past.[2–5] Systems that exploit vehicle flexibility for improved performance, such as vehicle roll control beyond aileron reversal and wing load alleviation have also been demonstrated.[6,7]

Considerably less data are available for supersonic cruise configurations. In the mid- to late-1990s, as part of the High Speed Research (HSR) program, research was performed in the areas of computational and experimental aeroelasticity.[8] As part of this research, aeroelastic wind-tunnel models were designed, built, and tested in the Transonic Dynamics Tunnel (TDT). A configuration of interest during the HSR program was the Technology Concept Aircraft (TCA) (see Figure 1). In order to experimentally simulate the aeroelastic behavior of the TCA, an aeroelastically-scaled semispan wind-tunnel model was designed referred to as the Semi-Span Super-Sonic Transport (S^4T).[9] Fabrication of the S^4T wind-tunnel model was initiated during the HSR program and continued (on a limited scope) even after the cancellation of the program.

Then, in 2006, the Supersonics Project was established under the NASA Fundamental Aeronautics Program (FAP). Under the Supersonics Project, the Aeroservoelasticity (ASE) Element was tasked with the modeling, analysis, and prediction of aeroelastic and ASE phenomena associated with supersonic configurations. It was under the ASE Element that fabrication of the S^4T wind-tunnel model was completed with plans to perform open- and closed-loop ASE wind-tunnel tests. The S^4T wind-tunnel model is a very sophisticated model that was designed so that it would flutter within the TDT operating boundary, making it an ideal testbed for investigating ASE issues associated with supersonic cruise configurations.

The S^4T wind-tunnel model was the subject of four wind-tunnel tests in the TDT: two open-loop (no feedback control) tests and two closed-loop (with feedback control) tests over the span of three years between 2007 and 2010. The goals of the open-loop tests were to acquire system identification data to enable the design of ASE control laws. The goals of the closed-loop tests were to evaluate several candidate ASE control laws in the performance of gust load alleviation (GLA), ride quality enhancement (RQE), and flutter suppression (FS) looking at both independent function as well as combined functions. A special session during the AIAA 2012 Structures, Structural Dynamics, and Materials (SDM) conference presents the various aspects of the S^4T wind-tunnel model program,[10–13] including the program overview that is the subject of this paper.

The paper begins with a brief description of the S^4T wind-tunnel model including design, instrumentation, and ground vibration tests. Details regarding TDT are available in the references[9] and will not be covered here. A description of the Computational Aeroelastic Models is then provided including linear and CFD models. Computational and experimental results are then presented in the Results section of the paper, followed by some Concluding Remarks.

II. S^{4}T Wind-Tunnel Model

II.A. Design

The process of aeroelastically scaling the full-size TCA to a size suitable for testing in the TDT will be briefly discussed in this section with greater detail available in the references.[10] Starting with the geometric and flight parameters for the TCA and then choosing the design condition in the tunnel, scale factors can be determined that would yield a model with aeroelastic characteristics easily scalable to the full-sized TCA. In order to ease the design, fabrication, and testing of the model, the maximum allowable size for the model in the TDT was determined by the TDT test section length limiting the model fuselage length to be 16 feet. This yielded a model length scale factor of just under 5%, based on the 326-foot length of the TCA. The chosen flight condition to be scaled was a TCA with a gross weight of 700,000 pounds at a cruise speed of Mach 0.95 (speed of sound of 1026 feet per second (fps)), and an altitude of roughly 22,500 feet and a dynamic pressure (q) of 540 pounds per square foot (psf). The Mach number was matched in the tunnel using a heavy gas medium that reduces the speed of sound to 548 fps and the dynamic pressure to 150 psf. Once the scale factors were determined, the vehicle components were then scaled so that model design could be initiated. Starting with the TCA finite element model (FEM), a scaling algorithm was developed to size the various components of the TCA.

The end result of this scaling algorithm was the S^{4}T wind-tunnel model, a sophisticated aeroelastic semi span wind-tunnel model designed and fabricated at NASA Langley with significant contributions from Boeing during the HSR program. The model is shown in Figure 2 mounted on a backstop in a model preparation area at the TDT in two different states of assembly. The photograph on the left of Figure 2 shows the model fully assembled as it would be in the tunnel. The photograph on the right of Figure 2 shows the model without the fuselage fairing installed and with key features highlighted. Those features are the three active surfaces (ride control vane, aileron, horizontal tail), flow-through nacelles with flexible attachments, and the flexible fuselage beam. The all-movable ride control vane (RCV) and the all-movable horizontal tail are mounted to the flexible beam. Linear piston hydraulic actuators, with a bandwidth of about 25 Hz, are used to deflect these control surfaces. Both surfaces have a peak-to-peak range of 30 degrees (+15 to -15).

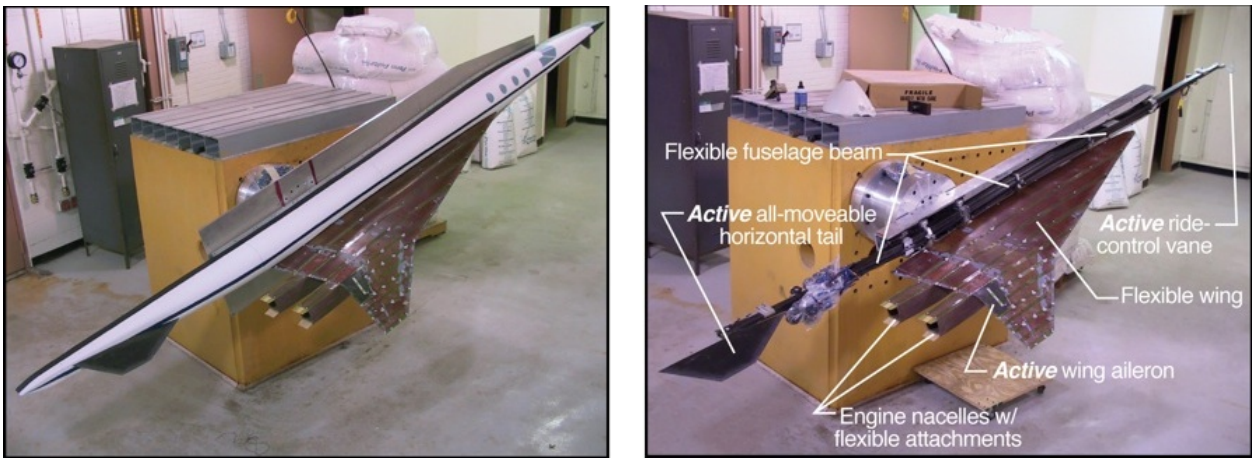

(a) Fully assembled model.

(b) Model without fuselage fairing installed.

Figure 2. Photographs of S^{4}T wind-tunnel model mounted on backstop.

The wind-tunnel model is 16.5 feet in length with a model span of 3.25 feet. The fuselage consists of a graphite-epoxy flexible beam (Figure 3) attached to an aluminum C-channel rigid beam and surrounded by a fiberglass-over-honeycomb fairing. In order to best mimic the flexibility of the fuselage, several sophisticated mounting mechanisms were designed and fabricated. These mounting mechanisms include attachment points that allow pitch and vertical motion of the flexible beam (along with minimal fore-aft motion) but constrain roll, yaw, and side motion. Two spring systems (referred to as nodal mounts) supply vertical stiffness through four U-springs (two springs per mount) shown in Figure 3. These nodal mounts can be locked with expansion spacers placed between the stop spacers on the U-springs for testing if a nearly cantilevered boundary condition is desired.

The wing consists of a fiberglass-epoxy skin over a honeycomb core and has a remotely controlled aileron

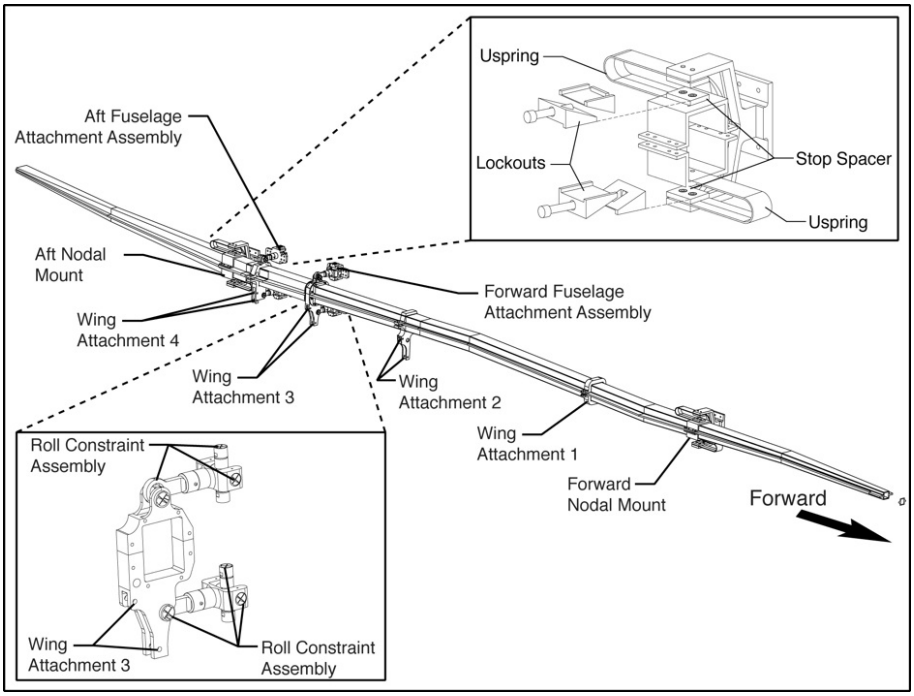

Figure 3. Fuselage beam showing attachment points and nodal mounts.

outboard of the engines. The wing root and tip chords are 82 inches and six inches, respectively. The wing attaches to the flexible fuselage beam at four locations through shear pins on the lower and upper surfaces of the wing. The wing's main spar is located between the aft two attachment points and runs out span wise to the wing tip. The aileron is constructed of graphite-epoxy skins over a honeycomb core and a balsa leading edge. A vane-type hydraulic actuator, also with a bandwidth of about 25 Hz, is used to deflect the aileron through a peak-to-peak range of 5 degrees (+2.5 to -2.5). An early conceptual drawing of the S^4T wind-tunnel model that highlights the primary hardware components is presented in Figure 4. Notice that on the wing, only the indicated control surface was realized.

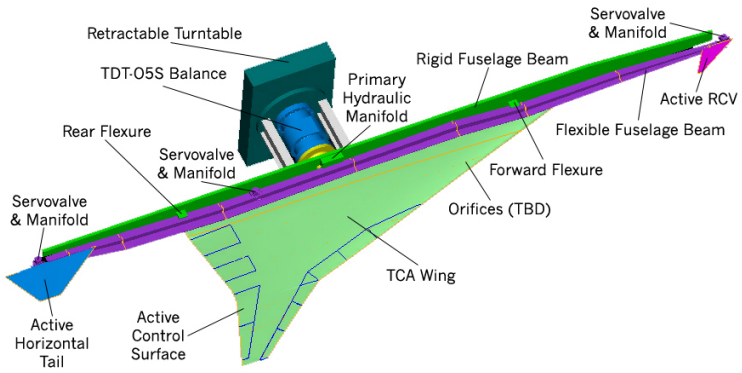

Figure 4. Drawing of S^4T wind-tunnel model without rigid fuselage fairing highlighting the primary hardware components.

II.B. Instrumentation

The instrumentation in the wing, illustrated in Figure 5, is extensive. The wing is populated with 26 accelerometers, the engines with four each (two on each inlet and two on each engine nacelle) , and the

fuselage with four. In addition, there are 93 unsteady pressure transducers on the wing (53 on the upper surface and 40 on the lower surface) arranged in six chord wise rows. Figure 6 contains the distribution of the wing pressure transducers with the left side of the figure corresponding to the upper surface and the right side of the figure corresponding to the lower surface. Volume constraints precluded the placement of pressure transducers and accelerometers at the leading and trailing edges of the outboard wing section. Additional instrumentation includes 12 strain gages (bending and torsion gages at three locations on the upper and lower surface), and additional torsional strain gages that measure ride-control-vane, aileron, and horizontal-tail positions. The flexible fuselage beam is instrumented with four accelerometers. The three servo-valves (one for each control surface actuator) were mounted on the flexible fuselage. An angle-of-attack sensor was installed on the rigid fuselage beam and used to measure angle of attack. A five-component sidewall balance (TDT-05S) was used to measure loads on only those components of the model connected to the rigid fuselage beam (RCV, wing, and horizontal tail). The components that were connected to the balance are referred to as the metric components. The fuselage fairing was connected to a plate that was connected to the turntable but not the balance. The fuselage fairing, therefore, was a non-metric component.

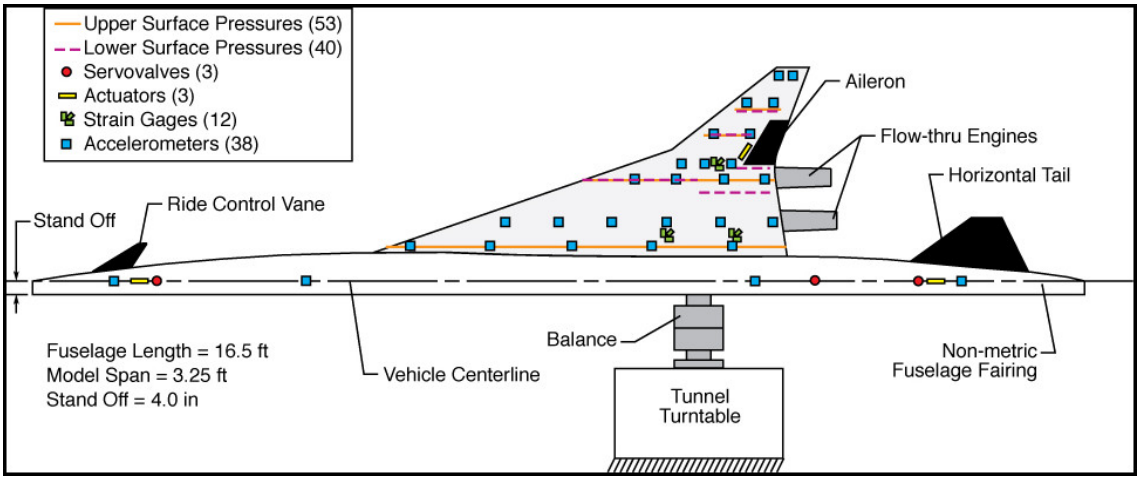

Figure 5. Model instrumentation layout.

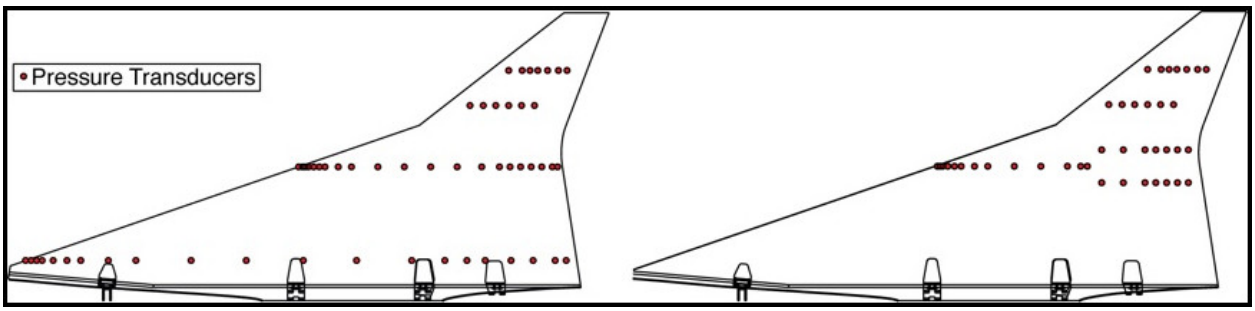

Figure 6. Wing unsteady pressure transducer locations; Left is upper surface, Right is lower surface.

III. Ground Vibration Tests

Several types of characterization measurements and tests were conducted on the wind-tunnel model prior to all four TDT wind-tunnel tests. These tests included mass and stiffness measurements, ground vibration tests (GVTs) on major model components and the fully assembled configuration, model geometry measurements, and actuator frequency response measurements. The results from these characterization tests were used for correlation with results from analysis. Where significant differences between measurement and prediction were identified, the analytical representations of the physical model, such as the finite element

model (FEM), were corrected. In this section, discussion will focus on results from GVTs. Details regarding all other characterization tests can be found in the references.[10]

Multiple GVTs were performed as an important component of each wind-tunnel test. Typically, one GVT was performed prior to every wind-tunnel test followed by another GVT at the end of the wind-tunnel test. Early in the program, a GVT was performed on major components separately such as the wing and the flexible fuselage. The data from these separate component tests were used to update the analytical FEM. Table 1 presents a summary of GVT measurements for the first five modes from the most recent wind-tunnel test conducted in September of 2010. For the most part, frequencies compare well across the board with some variations in damping. The comparison of measured frequencies with those from the updated FEM is also good. Additional details regarding the FEM are discussed in the next section of this paper.

	Pre-Test in Lab		Pre-Test in TDT		Post-Test in TDT		NASTRAN
Mode	Frequency	Damping	Frequency	Damping	Frequency	Damping	Frequency
1	6.395	3.547	6.375	5.465	6.249	3.909	6.290
2	8.089	2.285	7.935	2.227	7.838	1.795	8.435
3	10.323	3.518	10.312	2.616	10.059	2.889	10.074
4	11.635	3.745	—	—	11.781	10.903	11.401
5	12.528	1.437	12.585	2.130	12.384	3.224	12.875

Table 1. Measured damping and frequency (Hz) summary and analytical frequencies for most recent wind-tunnel test.

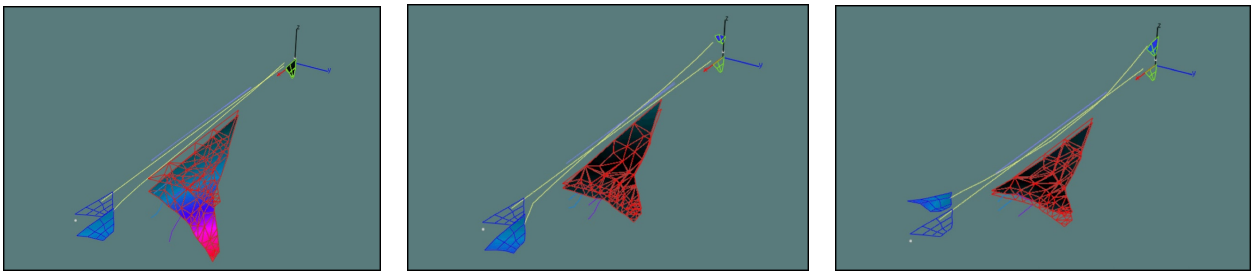

(a) First flexible measured mode (post-test).

(b) Second flexible measured mode (post-test).

(c) Third flexible measured mode (post-test).

Figure 7. Measured mode shapes of S^{4}T wind-tunnel model.

The first three measured flexible modes are presented in Figure 7. The first mode is predominantly a pitch mode about the forward nodal mount; the second mode is predominantly a pitch mode about the balance; and the third mode is predominantly a fuselage beam first bending. As will be shown in the next section, measured mode shapes compare well with those from the updated FEM.

IV. Computational Aeroelastic Models

A linear aeroelastic model of the S^{4}T wind-tunnel model was developed during the initial design of the wind-tunnel model as part of the HSR program. The structural portion of this linear aeroelastic model is a NASTRAN FEM consisting of beam and plate representations of 2711 nodes and 4105 elements depicted in Figure 8. The upper and lower surfaces are modeled as plate elements with proper outer mold line geometry definition. The fuselage is modeled as a series of beams and the engines are modeled as simple cruciforms. The first three flexible modes generated using the final updated NASTRAN FEM are depicted in Figure 9. The comparison of these analytical modes to the measured modes presented in the previous section is very good. The aerodynamic portion of the linear aeroelastic model of the S^{4}T wind-tunnel model was developed using linear subsonic (doublet lattice) and supersonic (ZONA51) unsteady aerodynamic theories. The aerodynamic box layout is shown in Figure 10.

Computational aeroelastic analyses using higher-order methods were performed for the S^{4}T wind-tunnel model using the CFL3D structured-grid aeroelastic CFD code using an inviscid and a viscous grid with 7 and 12 million grid points respectively. Both inviscid and viscous solutions were generated at several Mach numbers. The top figure of Figure 11 presents the CFL3D surface grid. It should be mentioned that initial

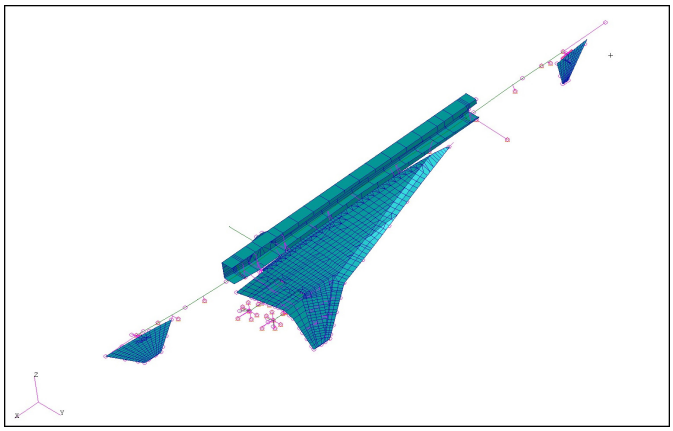

Figure 8. Finite element model.

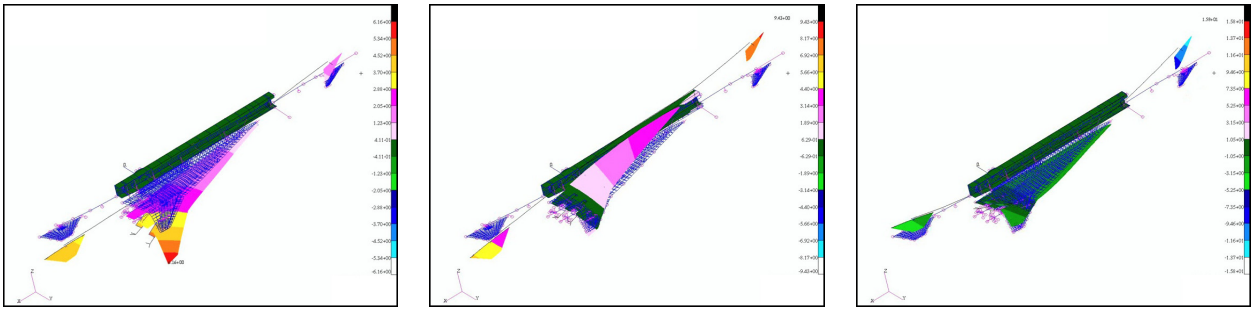

(a) First flexible analytical mode. (b) Second flexible analytical mode. (c) Third flexible analytical mode.

Figure 9. Analytical mode shapes of S^{4}T wind-tunnel model.

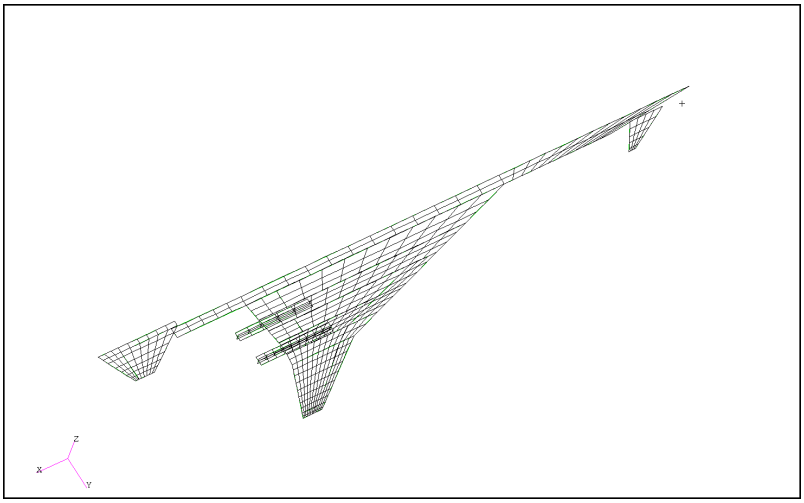

Figure 10. Aerodynamic box layout for linear aeroelastic analyses.

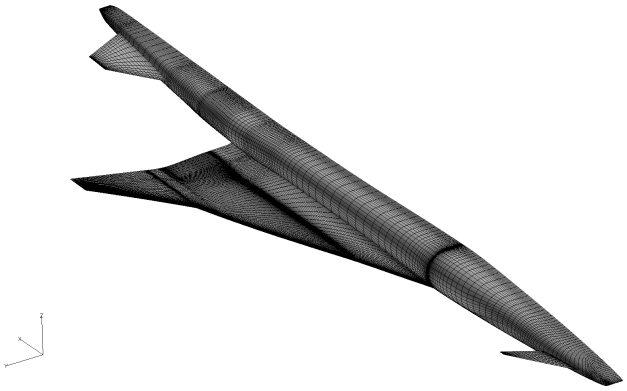

(a) CFL3D surface grid.

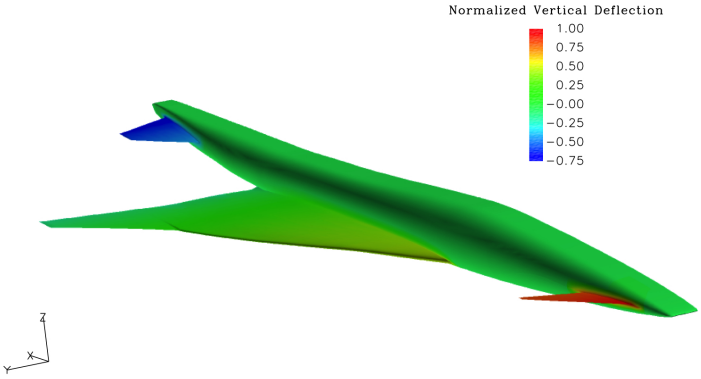

(b) Second mode vertical deflections.

Figure 11. CFL3D surface grid and second mode vertical deflections.

CFD steady analyses included the engines. However, for aeroelastic analyses, grids were generated without the engines in order to simplify the interpolation of the modes as well as to reduce the computational time to obtain an aeroelastic solution. Although inclusion of the engine aerodynamics slightly affected the steady results (8% difference in lift-curve slope), it was assumed that the engine aerodynamics would not have a significant impact on the aeroelastic response. Engine masses and inertias were, of course, included in the computation of the mode shapes.

The FEM flexible modes were interpolated onto the CFD viscous and inviscid surface grids. Although this is typically a complex process, the unique design of the S^4T wind-tunnel model made this interpolation process even more challenging. The main structural element of the wind-tunnel model is the flexible composite beam to which is attached the RCV, wing, and horizontal tail. Covering this flexible beam is a relatively rigid fiberglass fuselage shell that is attached directly to the angle-of-attack turntable (non-metric). Slots were designed into the fuselage shell to allow for the vertical translation of the RCV and horizontal tail due to deflection of the flexible beam. A gap between the wing and the fuselage shell allowed for the vertical movement of the wing. Transferring the mode shapes for the flexible beam to the computational fuselage surface would result in a fuselage shell with modal deflections which was not the case. A special procedure was developed that zeroed out the mode shapes on the majority of the fuselage shell while smoothly blending the mode shapes in the vicinity of the RCV, wing, and horizontal tail. Presented in the lower figure of Figure 11 is the vertical deflection of the RCV, wing, and horizontal tail due to the second flexible mode after the procedure was implemented. Additional details regarding the computational aeroelastic results for the S^4T wind-tunnel model can be found in the reference by Sanetrik.[11]

V. Active Controls

An important objective of this work was the demonstration of flutter-suppression, gust-load-alleviation, and ride-quality control laws, singly and in combination, over a range of Mach numbers and dynamic pressures. Control law designers were free to choose their own design methodologies and employ whatever sensors (accelerometers, strain gages) and active control surfaces (ride control vane, aileron, horizontal tail) they desired. Details regarding control law design and testing for the S^4T wind-tunnel model can be found in the reference by Christhilf.[13]

Some initial closed-loop performance goals were defined for each of the active controls functions prior to the first closed-loop test. After subsequent open- and closed-loop testing, some of these goals (or metrics) were altered to assure model safety. The initial goals are described below:

The goal of the flutter-suppression (FS) function was to increase the flutter dynamic pressure by an amount at least 44% above the open-loop flutter dynamic pressure while maintaining adequate relative stability. This minimum increase in dynamic pressure was to have been demonstrated across a range of Mach numbers.

The goal of the gust-load-alleviation (GLA) function was to decrease representative wing-load responses by an amount at least 20% below the open-loop responses while maintaining adequate relative stability. This minimum decrease in loads was to have been demonstrated across a range of Mach numbers. The naturally occurring tunnel turbulence (defined by power spectral density functions) was used as the gust excitation source.

The goal of the ride-quality-enhancement (RQE) function was to decrease representative fuselage acceleration responses by an amount at least 20% below the open-loop responses while maintaining adequate relative stability. This minimum decrease in accelerations was to have been demonstrated across a range of Mach numbers. The naturally occurring tunnel turbulence (defined by power spectral density functions) was used as the gust excitation source.

V.A. Controller Performance Evaluation

During closed-loop testing an online system was employed that provided valuable information about open- and closed-loop stability and performance. The generic name given to this system is controller performance evaluation or CPE.[14] Its open-loop capabilities included verification of the control law loaded into the digital controller and its closed-loop capabilities included prediction of closed-loop system stability. Its closed-loop capabilities included determining the relative stability of a given closed-loop system by evaluating the singular values of the return difference matrices and determining the open-loop plant stability to ascertain the open-

loop flutter boundary while operating closed-loop. Details regarding this method and its application to the S^{4}T wind-tunnel model can be found in the reference by Wieseman.[12]

V.B. Simulation

A valuable tool that was developed in support of the closed-loop testing was a simulation of the various available S^{4}T wind-tunnel model plant models and candidate control laws in the Simulink©-based Simulation Architecture for Evaluating Controls for Aerospace Vehicles (SAREC-ASV)[15] simulation framework. A schematic of the various user options available in this tool is presented as Figure 12. The simulation was able to host the discretized state space control laws in a form identical to that used for implementation in the wind tunnel. That capability allowed for screening and enforcement of a standardization of channel sequence, channel names, and physical units.

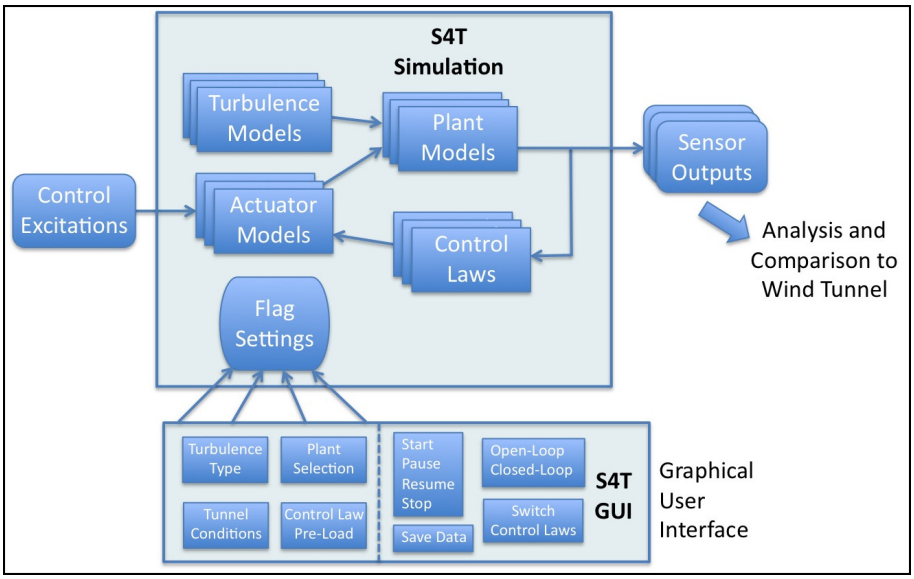

Figure 12. Schematic of data flow for the SAREC-ASV simulation tool.

Candidate excitation signal types, amplitudes and frequency content could be tried in simulation prior to use during wind tunnel testing, and the resulting time histories subjected to the same analysis techniques as were applied to both open- and closed-loop testing in the wind tunnel. Since the simulation for each case that was analyzed was based on a known analytical model, a comparison of frequency responses estimated from time histories, with and without simulated turbulence, was useful for providing pre-test insights with regards to the overall performance of the plant and candidate control law. The Graphical User Interface (GUI) developed for this simulation tool provided a very convenient interface for evaluation of multiple plant models, various turbulence models, and multiple control laws. The simulation was also useful for indicating whether a given control law would have a tendency to reach actuator rate saturation, and possible instability, in the presence of simulated turbulence even for cases that were closed-loop stable and robust according to linear analysis.

VI. Results

In this section, a summary of computational and experimental results is provided. The S^{4}T wind-tunnel model was tested four times in the TDT: two open-loop tests and two closed-loop tests. The purpose of the two open-loop tests was to gain familiarity with the model's performance and to acquire system identification data for development of transfer functions to be used subsequently in control law designs. In order to provide a well-defined test plan, it was decided to acquire data and test control laws at three Mach numbers: 0.80, 0.95, and 1.10. Therefore, most of the computational and experimental results to be presented will be at those three Mach numbers.

VI.A. Computational Results

Computational results consisted of linear flutter analyses using the NASTRAN model while CFD-based aeroelastic responses and flutter solutions were computed using the CFL3Dv6.4 code.[16–18] The CFL3Dv6.4 code solves the three-dimensional, thin-layer, Reynolds averaged Navier-Stokes equations with an upwind finite volume formulation.

As previously discussed, the S^{4}T wind-tunnel model fuselage fairing does not exhibit any motions while the lifting surfaces (RCV, wing, and horizontal tail) are the only surfaces that do exhibit aeroelastic motion. Due to the nature of this configuration, special consideration had to be given to the modal interpolation associated with the interface at the root where the lifting surfaces are in close proximity to the fuselage fairing. As a result, CFD plots and movies will indicate variations and motions only for the three lifting surfaces and none for the fuselage fairing, consistent with the actual wind-tunnel model.

Figure 13 presents the linear (NASTRAN) flutter dynamic pressures for several Mach numbers. Linear results indicate a slightly decreasing flutter dynamic pressure for most subsonic Mach numbers followed by rapid increases in the flutter dynamic pressure at the supersonic Mach numbers. These results were generated using measured damping values (see Table 1).

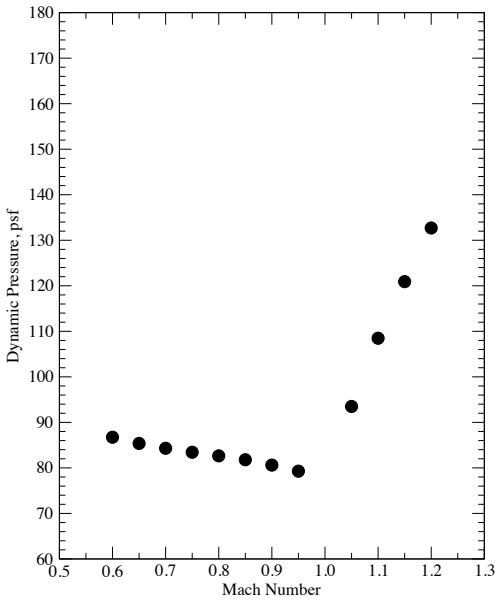

Figure 13. Linear (NASTRAN) flutter dynamic pressure predictions with measured damping values.

A sample of aeroelastic responses obtained using the CFL3D code[19] are presented in Figure 14. The figure on the left of Figure 14 presents the generalized displacement for the first flexible mode at four different dynamic pressures at a Mach number of 0.95 based on solution of the Euler (inviscid) equations. As indicated, the inviscid solution at this Mach number is neutrally stable at about 45 psf. Typically, inviscid CFD solutions yield shocks that are stronger and farther aft than when viscous effects are included. As a result, an unrealistically steep drop in the flutter dynamic pressure at certain Mach numbers for inviscid solutions is typical.

The figure on the right of Figure 14 presents the generalized displacement for the first flexible mode at four different dynamic pressures at a Mach number of 0.95 based on solution of the Navier-Stokes (viscous) equations. As would be expected, the inclusion of viscosity increases the flutter dynamic pressure to a more realistic value over the flutter dynamic pressure from the inviscid solution. Subsequent CFL3D analyses were performed including viscosity in order to generate physically-realistic aeroelastic responses. These results were generated prior to having measured damping values and are, therefore, based on an assumed 1% structural damping and are shown here for illustrative purposes only.

Various sensitivity analyses were performed using the CFL3D code. One of those sensitivity analyses was the effect of angle of attack on the aeroelastic stability at a Mach number of 0.95 and a dynamic pressure

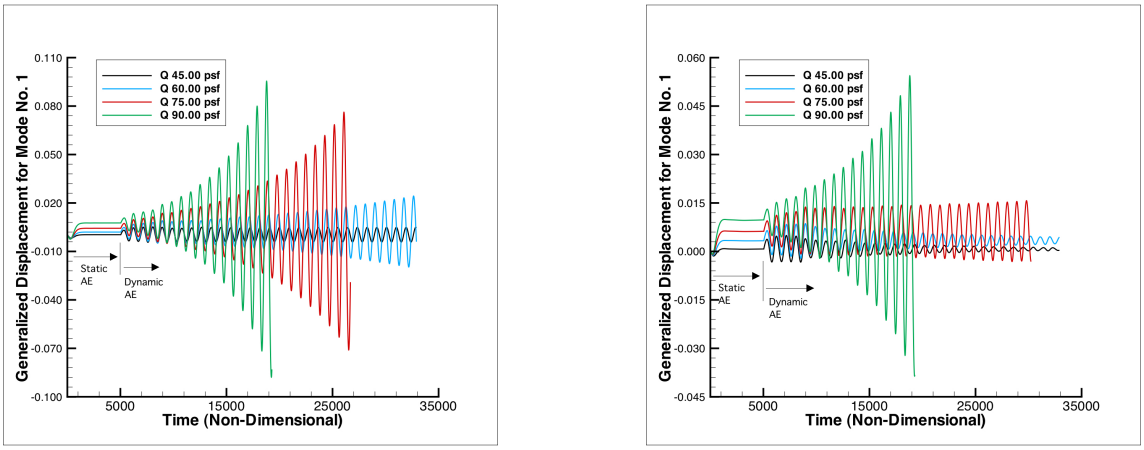

(a) Euler (inviscid) equations.

(b) Navier-Stokes (viscous) equations.

Figure 14. CFL3D response of first mode generalized displacement for different dynamic pressures at M=0.95 with an assumed 1% structural damping.

of 60 psf. Although not shown in this paper, a decrease in the angle of attack, especially near zero and at the negative angles of attack, resulted in decreased aeroelastic stability. As a result, some computational difficulties were encountered when computing aeroelastic responses at zero and negative angles of attack. Details are presented in the references.[11,19]

Recent CFL3D analyses performed at other Mach numbers (other than M=0.80, 0.95, and 1.10) have not yet identified a clear transonic flutter dip. Prior experience[8] has indicated that supersonic configurations, by design, tend to have a very narrow transonic range which can lead to a very narrow ('chimney') transonic flutter dip. Additional analyses are currently underway to see if such a boundary is characteristic of the S^{4}T wind-tunnel model.

Updated flutter dynamic pressures using measured damping values (see Table 1) from a post-test GVT are presented in Figure 15 for Linear (MSC-Nastran) analyses, Nonlinear (viscous CFL3D) analyses, and Experiment (last of the four tests). As can be seen, the overall trend between the linear and nonlinear results is similar for subsonic and supersonic Mach numbers. For subsonic Mach numbers, the CFL3D flutter dynamic pressures show better correlation with the experimental flutter dynamic pressures than the flutter dynamic pressures predicted by the linear analysis. Although the linear analysis is conservative, it is not clear why the linear results do not show better correlation. Sanetrik[11] discusses possible reasons for this discrepancy in the linear results. At supersonic Mach numbers, again the flutter dynamic pressures predicted by the linear analysis are lower than the flutter dynamic pressures predicted by CFL3D analysis. However, no flutter was measured during tests at supersonic Mach numbers. The highest dynamic pressure attainable during testing at M=1.10 was 101 psf. The experimental identification of the subsonic open-loop flutter boundaries and the issues associated with the inability to identify supersonic flutter boundaries is discussed in the Experimental Results section of the paper.

Development of aeroelastic reduced-order models (ROMs) was performed using CFL3D viscous solutions.[20,21] These ROMs can be used within a MATLAB/Simulink environment to rapidly create root locus plots that exhibit the migration of the aeroelastic roots. Presented in Figure 16 is a root locus plot at a Mach number of 0.95 indicating the coalescence of the first and second modes leading to flutter at a dynamic pressure of 86.4 psf with structural damping values measured from GVT (Table 1). It is important to mention that the primary expense associated with the generation of an aeroelatic ROM is a single CFL3D solution. The data generated by that single CFL3D solution is then post-processed within minutes to generate unsteady aerodynamic and aeroelastic ROMs from which root locus plots can be generated quickly and efficiently. As a point of interest, the root locus plot presented in Figure 16 has roots computed at eleven dynamic pressures ranging from 0 psf to 144 psf. While this root locus plot is generated in seconds, using the standard CFL3D solution approach would require a separate CFL3D solution for each dynamic pressure (eleven separate, lengthy, expensive CFL3D solutions). A comparison of all the predicted (Linear, CFL3D, and ROM) and experimental flutter boundaries is presented in Figure 17. Comparison of the ROM results at this Mach number and the supersonic Mach number with those from the full CFL3D viscous solutions

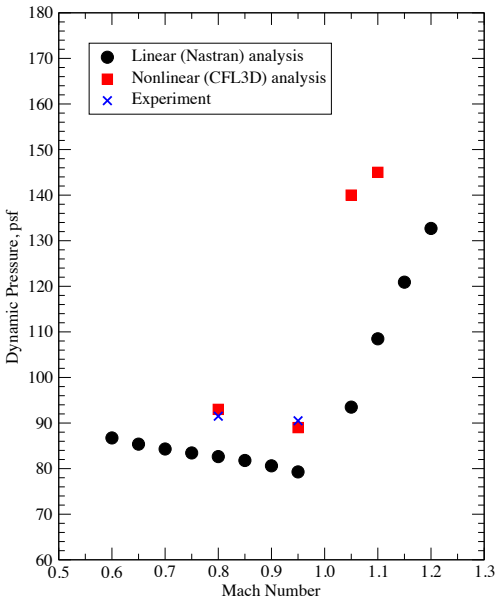

Figure 15. Summary of computational flutter boundaries using GVT measured damping values and comparison to experiment.

is very good. There appears to be a discrepancy in the comparison at M=0.80 between the full CFL3D solution and the ROM solution that is currently under investigation. Development of ROMs at additional Mach numbers is currently underway.

VI.B. Experimental Results

In this section, experimental results from both closed-loop tests are briefly presented. Details regarding control law designs and performance (including control power and actuator activity) are provided in the references.[22–29]

Although closed-loop testing of the S^4T wind-tunnel model yielded large amounts of valuable data and experience, it was difficult to meet the proposed closed-loop goals originally stated. As testing experience was gained, it became very obvious that model safety had to take priority over meeting initial closed-loop goals. That is, in several instances during closed-loop testing, it would have been possible to push a particular control law beyond a flight condition in order to achieve the initial goals. However, the complexity of the S^4T wind-tunnel model, in particular its control surfaces and actuators, made it clear to the entire test team that any attempt to reach the initial goals would endanger the safety of the model. These model safety limitations included measured closed-loop gains, minimum singular values, and overall motion of the model. This safety-minded approach, however, is consistent with the initial goals that included the requirement to "maintain adequate relative stability".

One important closed-loop goal that was achieved was to be able to perform multiple control modes (Gust Load Alleviation (GLA), Ride Quality Enhancement (RQE), and Flutter Suppression (FS)) simultaneously. Several control laws were designed specifically to perform in this fashion and did so successfully. In terms of GLA, a sample result from the first closed-loop test is presented on the left figure of Figure 18 as vertical shear versus dynamic pressure for open- and closed-loop measurements. The vertical shear was computed from a calibration of wing strain gauges. As can be seen, for this particular GLA control law, the measured vertical shear was reduced by 23% at the highest dynamic pressure.

Similarly, a sample result from the first closed-loop test for RQE is presented on the right figure in Figure 18 as aft fuselage acceleration versus dynamic pressure for open- and closed-loop measurements. As shown in the figure, a 26% reduction in the aft fuselage acceleration was achieved at the highest dynamic pressure tested (60 psf). For this particular condition and control law, the goal of a reduction in wing load responses by at least 20% was achieved while maintaining adequate relative stability.

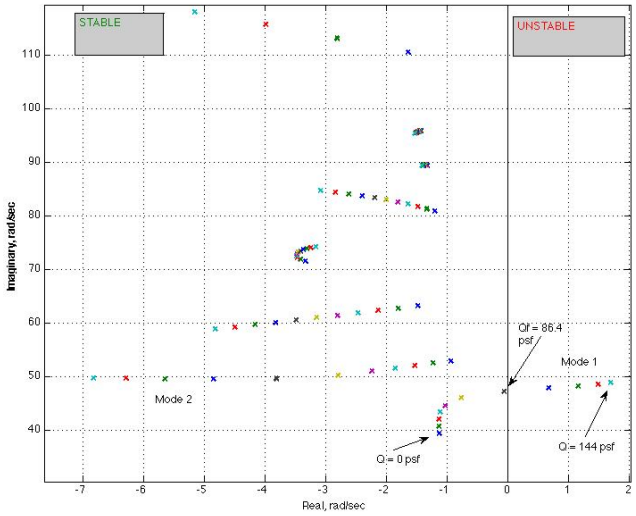

Figure 16. Root locus plot from aeroelastic ROM analysis, M=0.95, GVT-measured structural damping values.

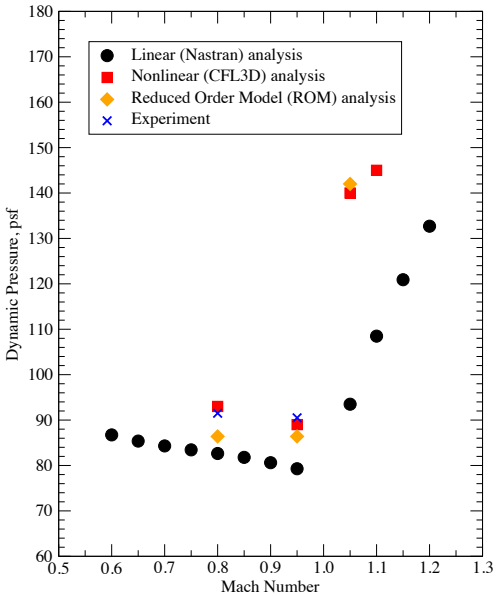

Figure 17. Summary of computational flutter boundaries using GVT measured damping values and comparison to experiment.

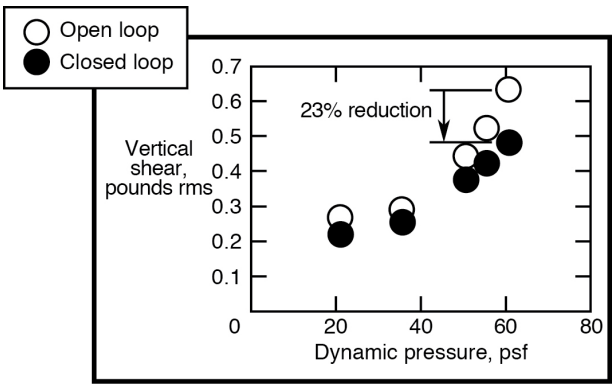

(a) Gust load alleviation (GLA) control law.

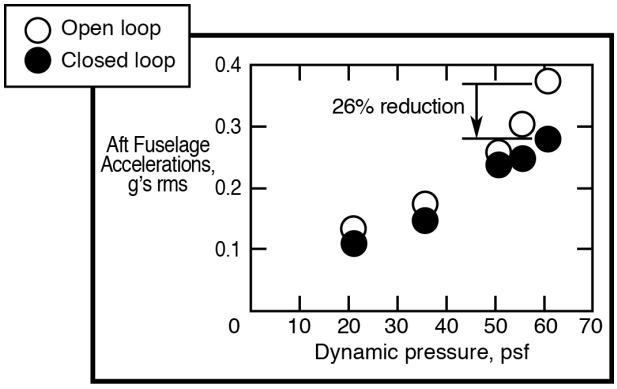

(b) Ride quality enhancement (RQE) control law.

Figure 18. Measured responses at M=0.80.

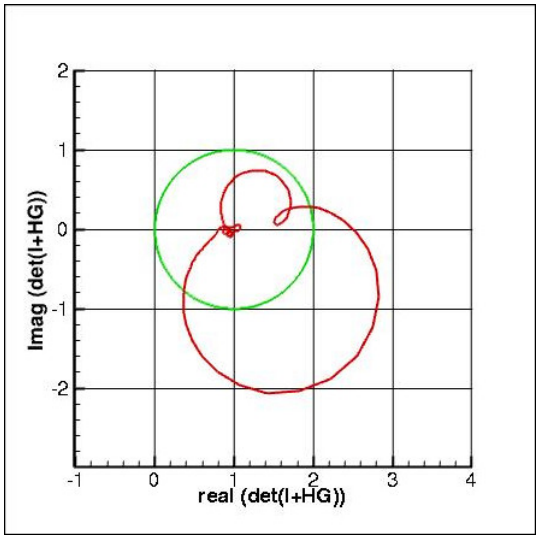

Figure 19. Nyquist plot at Mach number 0.80 and a dynamic pressure of 79 psf.

The focus of the first closed-loop test was on the validation of GLA and RQE control laws. Although some FS was attempted during this test, there was not enough time to carry out this phase of testing in a safe manner. Therefore, the second closed-loop test was focused on FS only. In order to perform FS safely, the CPE method described previously was used to identify an open-loop instability while the model was closed-loop stable. This was performed using Nyquist stability criteria.

Nyquist stability criteria, as represented by Nyquist plots, enables the identification of an open-loop instability using data acquired while the model is closed-loop stable. This provided a very safe method for identifying the open-loop flutter dynamic pressures as the actual encounter of a potentially destructive flutter point was avoided. Presented in Figure 19 is a Nyquist plot acquired from the simulated closed-loop system at M=0.80 and a dynamic pressure below the open-loop flutter point. As can be seen, there are no encirclements of the origin, indicating a stable open-loop system. It can be seen, however, that an encirclement may be approaching.

Figure 20 presents a simulated Nyquist plot at an even higher dynamic pressure clearly showing an encirclement, indicating that the system is no longer open-loop stable. During the test, however, Nyquist plots were generated based on measured data. The information gleaned from those plots was used to make decisions whether to continue increasing dynamic pressure. Due to limited space, samples of those plots are not presented in this paper. For demonstration purposes, sample Nyquist plot results were generated using simulated data. Results using measured data can be found in the reference by Wieseman.[12]

Presented in Figure 21 is a plot of flutter dynamic pressure versus Mach number with the flutter dynamic

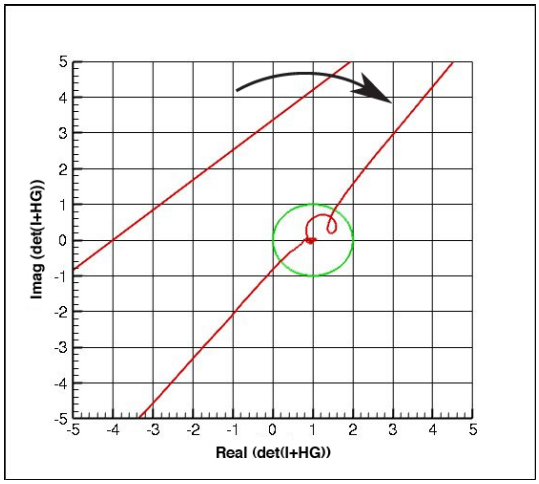

Figure 20. Nyquist plot, Mach number of 0.80 and a dynamic pressure of 89 psf.

pressures identified for Mach numbers of 0.80 and 0.95 using the Nyquist method described above. With the system closed-loop stable, a dynamic pressure of 95 psf was reached. Analysis of Nyquist plots indicated an open-loop instability of 93 psf for Mach number of 0.80 and 91.75 for Mach number of 0.95. Also presented in the plot is the highest attainable dynamic pressure of about 101 psf at Mach number of 1.10 that was reached with the system closed-loop stable. Based on the lack of an open-loop encirclement up to this dynamic pressure, the indication is that the open-loop flutter point at this Mach number is above the 101 psf condition. Again, due to model safety concerns, it was decided not to go beyond the 101 psf in order to find the open-loop flutter point. The primary concern at this condition is the possible existence of a transonic flutter dip somewhere between a Mach number of 0.95 and 1.10. If so, then due to the nature of TDT operations, a region of high instability could be encountered on the way back down from Mach number of 1.10 for a dynamic pressure higher than the 101 psf. For this reason, the identification of the open-loop flutter point at a higher dynamic pressure was not pursued.

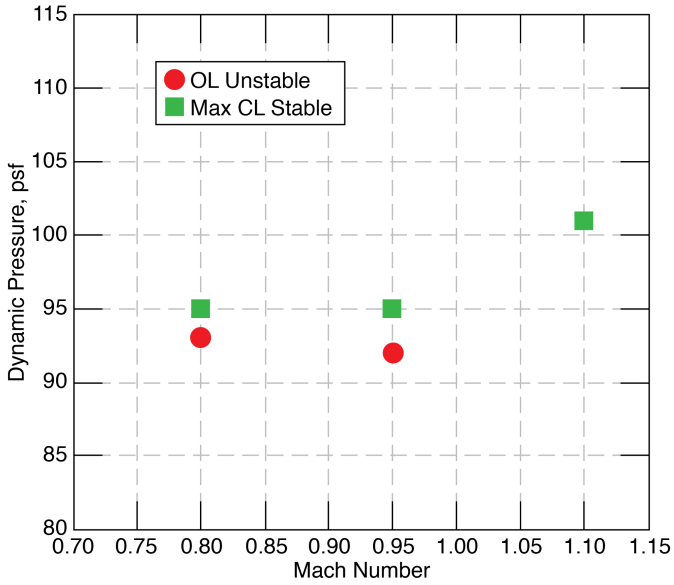

Figure 21. Identification of open-loop flutter dynamic pressures for Mach numbers of 0.80, 0.95, and 1.10.

VII. Concluding Remarks

A brief summary of computational and experimental results were presented for the SemiSpan SuperSonic Transport (S^4T) wind-tunnel model tested in the Transonic Dynamics Tunnel on four different occasions (two open-loop tests, two closed-loop tests) between 2007 and 2010. A description of the wind-tunnel model including primary hardware and associated test hardware was provided including a description of a closed-loop simulation tool, and the controller performance evaluation (CPE) system. Computational results included linear aeroelastic analyses using NASTRAN and nonlinear aeroelastic responses using the CFL3D aeroelastic code. Also presented was a sample root locus result obtained from the application of reduced-order modeling (ROM) methods developed at NASA. The experimental results presented included samples of results from evaluation of Gust Load Alleviation (GLA), Ride Quality Enhancement (RQE), and Flutter Suppression (FS) control laws. The successful application of an experimental Nyquist stability criterion in order to identify the open-loop flutter points while maintaining closed-loop stability was also presented. An important lesson learned from these analyses and experiments is that the identification of flutter boundaries for supersonic configurations may be elusive. That is, although linear and nonlinear analyses presented similar flutter boundary trends, a transonic flutter dip has not been identified to date. If, based on prior experience, this transonic flutter dip is very narrow, it could pose a hidden and serious risk within the flight envelope. Additional analyses and experiments are certainly required to completely understand the aeroelastic response of supersonic configurations.

References

[1] "Advanced Aeroservoelastic Testing and Data Analysis," *AGARD Conference Proceedings 566, NATO*, November 1995.

[2] Noll, T. E., "Aeroservoelasticity," *31st AIAA/ASME/ASCE/AHS/ASC Structures, Structural Dynamics and Materials Conference*, No. 1990-29359, Long Beach, CA, April 1990.

[3] Sandford, M. C., Abel, I., and Gray, D. L., "Development and Demonstration of a Flutter-Suppression System Using Active Controls," *NASA TR R-450*, 1975.

[4] Abel, I., Perry, B., and Newsom, J. R., "Comparison of Analytical and Wind-Tunnel Results for Flutter and Gust Response of a Transport Wing with Active Controls," *NASA TP 2010*, 1982.

[5] Waszak, M. R., "Robust Multivariable Flutter Suppression for the Benchmark Active Control Technology (BACT) Wind-Tunnel Model," *Eleventh Symposium on Structural Dynamics and Control*, May 12-14 1997.

[6] Multiple, "Special Section: Active Flexible Wing," *Journal of Aircraft*, Vol. 32, January-February 1995.

[7] Pendleton, E. W., Bessette, D., Field, P. B., and Miller, G. D., "Active Aeroelastic Wing Flight Research Program Technical Program and Model Analytical Development," *Journal of Aircraft*, Vol. 37, July-August 2000.

[8] Silva, W. A., Keller, D. F., Florance, J. R., Cole, S. R., and Scott, R. C., "Experimental Steady and Unsteady Aerodynamic and Flutter Results for HSCT Semispan Models," *AIAA/ASME/ASCE/AHS/ASC 41st Structures, Structural Dynamics, and Materials Conference*, No. 2000-1697, April 2000.

[9] Perry, B., Silva, W. A., Florance, J. R., Wieseman, C. D., Pototzky, A. S., Sanetrik, M. D., Scott, R. C., Keller, D. F., Cole, S. R., and Coulson, D. A., "Plans and Status of Wind-Tunnel Testing Employing an Aeroservoelastic Semispan Model," *48th AIAA/ASME/ASCE/AHS/ASC Structures, Structural Dynamics, and Materials Conference*, No. 2007-1770, Honolulu, HI, April 23-26 2007.

[10] Florance, J. R., Scott, R. C., Keller, D. F., Sanetrik, M. D., Funk, C. J., and Silva, W. A., "Lessons in the Design and Characterization Testing of the Semi-Span Super-Sonic Transport (S^4T) Wind-Tunnel Model," *53rd AIAA/ASME/ASCE/AHS/ASC Structures, Structural Dynamics and Materials Conference*, Honolulu, HI, April 2012.

[11] Sanetrik, M. D., Silva, W. A., and Hur, J., "Computational Analysis of the Semi-Span Super-Sonic Transport (S^4T) Configuration," *53rd AIAA/ASME/ASCE/AHS/ASC Structures, Structural Dynamics and Materials Conference*, Honolulu, HI, April 2012.

[12] Wieseman, C. D. and Christhilf, D. M., "Analytical and Experimental Evaluation of Digital Control Systems for the Semi-Span Super-Sonic Transport (S^4T) Project," *53rd AIAA/ASME/ASCE/AHS/ASC Structures, Structural Dynamics and Materials Conference*, Honolulu, HI, April 2012.

[13] Christhilf, D. M., Roughen, K. M., Moulin, B., Ritz, E., Chen, P. C., and Perry, B., "Characteristics of Control Laws Tested on the Semi-Span Super-Sonic Transport (S^4T) Wind-Tunnel Model," *53rd AIAA/ASME/ASCE/AHS/ASC Structures, Structural Dynamics and Materials Conference*, Honolulu, HI, April 2012.

[14] Pototzky, A. S., Wieseman, C. D., Hoadley, S. T., and Mukhopadhyay, V., "On-Line Performance Evaluation of Multiloop Digital Control Systems," *Journal of Guidance, Control, and Dynamics*, Vol. 15, July-August 1992, pp. 878–884.

[15] Christhilf, D. M., Pototzky, A. S., and Stevens, W. L., "Incorporation of SemiSpan SuperSonic Transport (S4T) Aeroservoelastic Models into SAREC-ASV Simulation," *AIAA Guidance, Navigation, and Control Conference*, No. 2010-8099, Toronto, CA, Aug. 2010.

[16] Krist, S. L., Biedron, R. T., and Rumsey, C. L., "CFL3D User's Manual (Version 5.0)," *NASA TM*, No. 1998-208444, June 1998.

[17] Bartels, R. E., "Mesh Strategies for Accurate Computations of Unsteady Spoiler and Aeroelastic Problems," *AIAA Journal of Aircraft*, Vol. 37, 2000, pp. 521–525.

[18]Bartels, R. E., Rumsey, C. L., and Biedron, R. T., "CFL3D Version 6.4: General Usage and Aeroelastic Analysis," *NASA TM 2006 214301*, April 2006.

[19]Hur, J., "Aeroelastic Analysis of SemiSpan SuperSonic Transport (S4T) Wind-Tunnel Model for Transonic Speeds," *NASA CR, In progress*, 2012.

[20]Silva, W. A., "Simultaneous Excitation of Multiple-Input/Multiple-Output CFD-Based Unsteady Aerodynamic Systems," *Journal of Aircraft*, Vol. 45, No. 4, July-August 2008, pp. 1267–1274.

[21]Silva, W. A., "Recent Enhancements to the Development of CFD-Based Aeroelastic Reduced Order Models," *48th AIAA/ASME/ASCE/AHS/ASC Structures, Structural Dynamics, and Materials Conference*, No. 2007-2051, Honolulu, HI, April 23-26 2007.

[22]Roughen, K., Bendiksen, O., and Gadient, R., "Active Aeroelastic Control of the Supersonic Semispan Transport (S4T) Model," *AIAA Guidance, Navigation, and Control Conference*, No. 2010-8397, Toronto, CA, Aug. 2010.

[23]Roughen, K., Bendiksen, O., and Gadient, R., "Active Aeroelastic Control of the Supersonic Semispan Transport (S4T) Model," *51st AIAA Structures, Structural Dynamics, and Materials Conference*, No. 2010-8397, Orlando, FL, April 2010.

[24]Hammerand, D., Gariffo, J., Roughen, K., Baker, M., and Bendiksen, O., "Generation of Aeroservoelastic Reduced Order Models Using Time Scaling," *51st AIAA Structures, Structural Dynamics, and Materials Conference*, No. 2010-2947, Orlando, FL, April 2010.

[25]Roughen, K. and Bendiksen, O., "Development of Generalized Aeroservoelastic Reduced Order Models," *50th AIAA Structures, Structural Dynamics, and Materials Conference*, No. 2009-2491, Palm Springs, CA, April 2009.

[26]Roughen, K., "Active Aeroelastic Control of Supersonic Transport Aircraft," *PhD Dissertation*, University of California, Sept. 2009.

[27]Chen, P. C., Moulin, B., Ritz, E., Lee, D. H., and Zhang, Z., "CFD-Based Aeroservoelastic Control for Supersonic Flutter Suppression, Gust Load Alleviation, and Ride Quality Enhancement," *50th AIAA Structures, Structural Dynamics, and Materials Conference*, No. 2009-2537, Palm Springs, CA, April 2009.

[28]Moulin, B., Ritz, E., Chen, P. C., Lee, D. H., and Zhang, Z., "CFD-Based Control for Flutter Suppression, Gust Load Alleviation, and Ride Quality Enhancement for the S4T Model," *51st AIAA Structures, Structural Dynamics, and Materials Conference*, No. 2010-2623, Orlando, FL, April 2010.

[29]Moulin, B., Ritz, E., Florance, J. R., Sanetrik, M. D., and Silva, W. A., "CFD-Based Classic and Robust Aeroservoelastic Control for the SuperSonic SemiSpan Transport Wind-Tunnel Model," *AIAA Guidance, Navigation, and Control Conference*, No. 2010-7802, Toronto, CA, Aug. 2010.